Supporting Information for

Tannic Acid as a Multifunctional Bridge Driving Structural Ordering and Surface Passivation of ZnO for Over 20% Efficiency Inverted Solar Cells with Improved Stability

Yurong He,[a] Wentao Miao,[a] Jianhua Han,*[b] Wenyang Luo,[a] Zhuang Li,[a] Jin Chen,[a] Liangliang Chen,[a] Xunchang Wang,*[a] Renqiang Yang*[a]

[a] Y. He, W. Miao, W. Luo, Z. Li, J. Chen, Dr. L. Chen, Dr. X. Wang, Prof. R. Yang

Key Laboratory of Flexible Optoelectronic Materials and Technology (Ministry of Education), School of Optoelectronic Materials & Technology, Jianghan University, Wuhan 430056, China

E-mail: wangxc@jhun.edu.cn, yangrq@jhun.edu.cn

[b] Prof. J. Han

State Key Laboratory of Fine Chemicals, Frontier Science Center for Smart Materials, School of Chemical Engineering Dalian University of Technology, Dalian 116024, China

E-mail: hanjianhua@dlut.edu.cn

Materials and characterization

All the reagents, unless otherwise specified, were purchased from Sigma-Aldrich Co., J&K, and Tokyo Chemical Industry Co., Ltd., and were used without further purification. Tannin acid was purchased from J&K. PM6, L8-BO, D18, Y6, BTP-ec9 was purchased from Solarmer Materials Inc. All air and water-sensitive reactions were carried out under N_2.

Molecular Dynamic Analysis.

1) Density functional theory (DFT): All computations were performed with the Gaussian 16 program.

2) All density functional theory (DFT) calculations were performed using the Vienna ab initio simulation package (VASP) with plane-wave basis sets and the projector augmented-wave (PAW) method [1,2]. The exchange-correlation potential was described by the generalized gradient approximation (GGA) with the Perdew-Burke-Ernzerhof (PBE) functional. To account for van der Waals interactions, Grimme's DFT-D3 dispersion correction was employed. A ZnO (0 0 2) surface supercell consisting of 6 × 4 × 1unit cells was constructed to model the adsorption of the TA molecule. A vacuum layer of approximately 15 Å was introduced along the z-direction to minimize interactions between periodic images. The plane-wave energy cutoff was set to 450 eV, and Brillouin-zone integrations were performed using a Γ-centered 1 × 2 × 1 Monkhorst-Pack k-point mesh. Structural optimizations were carried out until the maximum force on each atom was less than 0.02 eV/Å, with an energy convergence criterion of 10^{-5} eV between successive self-consistent field iterations. The adsorption energy E_{ads} can be defined as:

$$E_{ads} = E_{*M} - E_{*} - E_{M}$$

where E_{*M} stands for the energy of the monolayer with the adsorbed M molecule, E_{*} is the energy of surface, and E_M is the energy of a M molecule under vacuum.

3) Molecular dynamics (MD): All-atom molecular dynamics (MD) simulations were performed using Materials Studio (BIOVIA, Dassault Systèmes, France). Molecular construction and visualization were carried out in the Visualizer module, while model packing using Amorphous Cell module, geometry optimization, energy calculations, and radial distribution function (RDF) analyses using Forcite modules.

To clarify the differences between the fragment model and the full-molecular adsorption, we have calculated the molecular dynamics (MD) simulation and investigated the interaction between the complete TA molecule

and ZnO. The calculated interaction energies are summarized in Table S1. The adsorption energy of TA molecule is -1231.8 kcal/mol, demonstrating a strong interaction between TA and ZnO. To quantify the contribution of each functional group, we split TA into three characteristic groups and calculated their interaction energies with ZnO separately: the pyrogallol group is -927.1 kcal/mol, the catechol group is -296.8 kcal/mol, and the carbonyl group contributes -7.86 kcal/mol. The contributions of the catechol and carbonyl groups are relatively weak. Therefore, the pyrogallol groups were utilized to simulate the effect of the adsorption process between TA and ZnO.

The radial distribution function (RDF) results indicate that the intact tannic acid molecules and their polyphenolic functional groups exhibit clear short-range ordered structures on the ZnO surface. The overall TA molecule and the pyrogallol group show a sharp main peak at approximately 3-4 Å, indicating that the pyrogallol group has a strong interaction with the surface and dominates the adsorption behavior. Although the catechol group exhibits a multi-peak distribution, the peak positions are slightly shifted towards a longer distance and the structure is more diffuse, suggesting a weaker interaction. In contrast, the carboxyl group shows no obvious sharp peak with a broad distribution, indicating weak interactions with the surface. As shown in the Figure S4, the equilibrium adsorption configuration further reveals that the TA molecules interact with ZnO in a parallel posture, with the polyphenolic hydroxyl groups facing the surface to form multiple-site coordination and hydrogen bond networks.

In conclusion, both the MD simulation and the DFT fragment calculation confirm that the strong adsorption between TA and ZnO is mainly driven by the phenolic hydroxyl group. These interactions effectively passivated the surface defects of ZnO and improve the structural order of ZnO.

Atomic force microscopy based infrared spectroscopy (AFM-IR)

AFM-IR measurements were conducted in tapping mode using a NanoIR3 system (Bruker Corporation, USA) equipped with a quantum cascade laser (QCL). AFM-IR is a photothermal technique that combines atomic force microscopy (AFM) and infrared spectroscopy, enabling unambiguous chemical identification of samples with spatial resolution on the tens of nanometers scale.

Scanning electron microscope (SEM)

The morphologies and microstructure of the as-prepared samples were observed using a field emission scanning electron microscope (FE-SEM, JEOL JEM-2200).

High-resolution transmission electron microscope (HR-TEM)

After preparing the solution, let it undergo ultrasonic treatment for 30 seconds, then apply it onto the copper mesh. After drying, conduct the test. The model of the instrument used in the field emission transmission electron microscope is FEI Tecnai G2 F20.

X-ray photoelectron spectra (XPS)

Films were spin-coated inside an argon-filled glovebox and dried before transfer to the XPS chamber. XPS signals were collected on the Thermo Fisher ESCALAB 250Xi scan XPS microprobe with Al Kα source.

Fourier transform infrared spectroscopy (FTIR)

The FTIR absorption spectra were performed on Infrared Spectrum Microscope (Nicolet is10 FT-IR spectrometer with diamond ATR crystals and a DTGS detector.). The measurement was based on a reflection mode.

Ultraviolet photoelectron spectroscopy (UPS)

Ultraviolet photoelectron spectrometer (UPS) measurement was performed by AXIS ULTRA DLD instrument of Kratos company.

Absorption spectra measurements.

UV-vis absorption spectra were carried out via Hitachi U-4100 spectrophotometer.

Raman spectra

Laser confocal microscope-Raman spectra were recorded on Thermo Scientific DXRxi (excitation wavelength = 532 nm).

Contact Angle.

The contact angle tests were performed on a contact angle meter (GBX DIGIDROP). The surface energy of the polymers was characterized and calculated by the contact angles of the two probe liquids using the Wu model (1): Wu model:

$$\gamma_{water}(1+cos\theta_{water}) = \frac{4\gamma_{water}^{d}\gamma^{d}}{\gamma_{water}^{d}+\gamma^{d}} + \frac{4\gamma_{water}^{p}\gamma^{p}}{\gamma_{water}^{p}+\gamma^{p}} \#(1)$$

$$\gamma_{oil}(1+cos\theta_{oil}) = \frac{4\gamma_{oil}^{d}\gamma^{d}}{\gamma_{oil}^{d}+\gamma^{d}} + \frac{4\gamma_{oil}^{p}\gamma^{p}}{\gamma_{oil}^{p}+\gamma^{p}}$$

$\gamma = \gamma^{d} + \gamma^{p} \#(2)$

where γ is the total surface tension of acceptor and polymers; γ^{d} and γ^{p} are the dispersion and polar components of γ; γ^{i} is the total surface tension of the i material (i = water or diiodomethane); γ_{i}^{d} and γ_{i}^{p} are the dispersion and polar components of γ_{i}; and θ_{i} is the droplet contact angle of the i material on the acceptor and polymers films.

Grazing Incidence Wide-Angle X-Ray Scattering.

2D-GIWAXS experiments were carried out on a GANESHA 300XL+ system from JJ X-ray. The instrument is equipped with a Pilatus 300K detector, with pixel size of 172 × 172 μm. The X-ray source is a Genix 3D Microfocus Sealed Tube X-Ray Cu-source with integrated Monochromator (30 W). The wavelength used is λ = 1.5418 Å. The detector moves in a vacuum chamber with sample-to-detector distance varied between 0.115 m and 1.47 m depending on the configuration used, as calibrated using silver behenate (d_{001} = 58.380 Å). The minimized background scattering plus high-performance detector allows for a detectable q-range varying from 3×10^{-3} to 3 $Å^{-1}$ (0.2 to 210 nm). The sample was placed vertically on the goniometer and tilted to a glancing angle of 0.2° with respect to the incoming beam. A small beam was used to get a better resolution. The accumulation time was 30 minutes for each measurement. In-plane and out-of-plane line-cuts were obtained using SAXSGUI program.

Atomic force microscopy (AFM) measurements.

Standard tapping-mode AFM measurements in ambient were performed on a Scanned Probe Imaging and Development (SPID) on Park NX-10. The AFM images were confirmed from different samples and scan areas. The root-mean-square roughness (RMS) values of the height images were obtained from the whole scan area (5 μm × 5 μm). All the AFM images were flattened and exported from the software.

Solar Cell Device Fabrication and Characterization.

The OSCs were fabricated with a device configuration of ITO/ETL/ active layer/MoO_X/Ag. The ITO-coated glass substrates were sonicated successively with detergent, deionized water, acetone and isopropanol, and dried with nitrogen flow. Then, the ITO substrates were treated by ultraviolet-ozone for 15 min. The ZnO

precursor was prepared by dissolving 1 g zinc acetate dihydrate and 280 μL ethanolamine in 20 mL of 2-methoxyethanol under stirring overnight for the hydrolysis reaction. For the hybrid ETL, add 3% of 1mg/ml TA ethanol solution. The ZnO/ ZnO (TA) solution was spin-coated onto ITO with 4000 rpm for 30 s as the electron transporting layer and then was annealed at 200°C for 1h. Then, the active layer was spin-coated in nitrogen glovebox. Finally, MoO_3 (10 nm) and Ag (100 nm) layers were prepared by vacuum evaporation under vacuum condition of 5×10^{-4} Pa, respectively.

We also spin-coated the TA solution onto the ZnO surface to prepare surface-passivated devices, and measured the photovoltaic performance. The PCE of the devices with surface-coated TA is 1.5%, which is much lower than that of the ZnO@TA devices (PCE of 20.1%). This comparative experiment further revealed that TA regulates the crystallization and defect states of ZnO at the bulk level rather than relying solely on surface modification to enhance device performance. Therefore, in this study, TA was added to the ZnO precursor solution for further investigation.

In this study, the different types of active layers were selected, including PM6:L8-BO, PM6:Y6, PM6: BTP-ec9 and D18:L8-BO. The detailed preparation methods of different active layers are depicted as follows:

PM6:L8-BO: The PM6: L8-BO ratio was kept at 1:1.2 (wt/wt) with the polymer donor of PM6 concentration of 7 mg mL^{-1} in chloroform, and the active layer solution was stirred at room temperature for 2 h. The 0.3 % CN was added as solvent additive in the active layer before spin coating of PM6: L8-BO, and then the mixed solution was spin-coated at 3000 rpm for 30 s in nitrogen glovebox. Subsequently, the active layers were thermally annealed at 85°C for 5 min.

PM6:Y6: The PM6:Y6 ratio was kept at 1:1.2 (wt/wt) with the polymer donor of PM6 concentration of 7 mg mL^{-1} in chloroform, and the active layer solution was stirred at room temperature for 2 h. The 0.5 % CN was added as solvent additive in the active layer before spin coating of PM6:Y6, and then the mixed solution was spin-coated at 3000 rpm for 30 s in nitrogen glovebox. Subsequently, the active layers were thermally annealed at 85°C for 5 min.

PM6:BTP-eC9: The PM6:BTP-eC9 ratio was kept at 1:1.2 (wt/wt) with the polymer donor of PM6 concentration of 7 mg mL^{-1} in chloroform, and the active layer solution was stirred at room temperature for 2 h. The 0.5 % DIO was added as solvent additive in the active layer before spin coating of PM6: BTP-ec9, and then the mixed solution was spin-coated at 3000 rpm for 30 s in nitrogen glovebox. Subsequently, the active layers were thermally annealed at 85°C for 5 min.

D18:L8-BO: The D18:L8-BO**:** ratio was kept at 1:1.2 (wt/wt) with the polymer donor of D18 concentration

of 7 mg mL^{-1} in chloroform, and the active layer solution was stirred at room temperature for 2 h. The 0.5 % DIO was added as solvent additive in the active layer before spin coating of PM6: BTP-ec9, and then the mixed solution was spin-coated at 3000 rpm for 30 s in nitrogen glovebox. Subsequently, the active layers were thermally annealed at 85°C for 5 min.

The current-voltage (*J-V*) characteristics were measured with a Keithley 2450 source measurement unit. The OSCs were measured under an irradiation intensity of 100 mW cm^{-2} (AM 1.5G) by a Newport solar simulator. The EQE spectra were analyzed using an integrated system (LST-QE). The highly sensitive EQE was measured by using an integrated system (PECT-600, Enlitech), where the photocurrent was amplified and modulated by a lock-in instrument.

Device stability test.

To evaluate the intrinsic chemical stability of TA molecule, we conducted aging experiments on the TA samples under the following four conditions: (1) a humid and hot environment (85 °C /40% RH); (2) in an inert atmosphere (N_2) with continuous illumination (AM 1.5G, 100 mW/cm^2); (3) continuous illumination in a humid and hot environment; (4) continuous heating at 100 °C in air. After the aging treatment, the molecular structure of TA was analyzed using nuclear magnetic resonance (NMR). As shown in the Figure S11, the characteristic peaks in the NMR spectra of TA under all aging conditions did not show any significant shift or splitting compared to the original sample, nor did any new degradation product peaks appear. These results indicate that the TA molecule itself is stable under long-term light and humid heat conditions, which could attribute to the improved stability in devices.

All devices were fabricated under optimized processing conditions. Devices for thermal stability test were placed in a glovebox filled with ultrahigh purity nitrogen without encapsulation and carried out on a hot plate with a continuous thermal stress of 85°C in dark condition. Second, the unencapsulated inverted devices was assessed under continuous 1-sun-equivalent LED illumination and maximum power point (MPP) tracking. In order to further determine the causes of aging, we conducted a statistical analysis of the photovoltaic parameters before and after aging, as shown in the Table S9. The results show that the enhanced stability is attributed to the effective suppression of degradation in short-circuit currents, fill factors, and open-circuit voltages.

The Analysis of J_{ph} vs V_{eff} Relationships.

The definition of J_{ph} is the difference between the current density under illumination (J_L) and the dark current density (J_D), with V_0 denoting the voltage at which J_{ph} equals zero. Consequently, V_{eff} is defined as the difference between V_0 and the applied voltage (V_{appl}). When V_{eff} reaches a high value (> 4V), it is normally believed that generated excitons are fully collected, in which J_{ph} is equal to saturated current density (J_{sat}). Then, we can calculate J_{SC}/J_{sat} and J_{max}/J_{sat} to describe exciton dissociation (η_{diss}) and charge collection (η_{coll}) efficiency. J_{max} is the J_{ph} at the maximal output point.

Electrochemical impedance spectroscopy (EIS) measurement.

The electrochemical S8 impedance spectroscopy (EIS) measurement was performed using Zennium-E at frequencies from 1 MHz to 10 Hz. A bias voltage equal to V_{OC} was applied to offset the total current.

Transient photocurrent (TPC), Transient Photovoltage (TPV)

TPC, TPV measurements were obtained from a platform namely PAIOS which contains the characterization of Solar Cells. The TPV is based on monitoring the photovoltage decay upon a small optical perturbation during different constant bias light-intensity (using the same white LED for TPC measurements) and under open-circuit condition. Variable bias light intensities lead to a range of V_{OC} to be studied. The photovoltage decay kinetics of all devices follows a mono-exponential decay: $\delta V = Aexp(-t/\tau)$ where t is the time and τ is the charge carrier lifetime.

Thermogravimetry Analysis (TGA)

Thermogravimetric analysis (TGA) was performed on Rigaku TG/DTA7300 (Japan) from 40 to 300 ^oC with a heating rate of 20 ^oC min^{-1} in N_2 atmosphere.

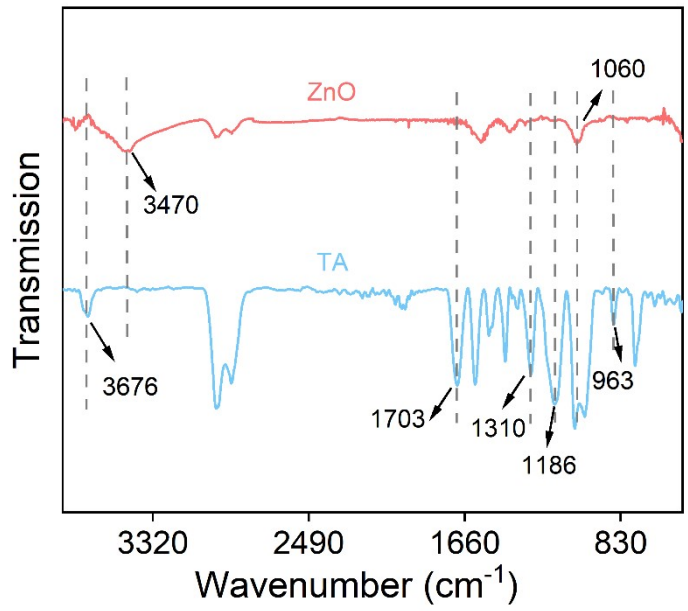

Figure S1. Fourier transform infrared spectroscopy of tannic acid film and ZnO film.

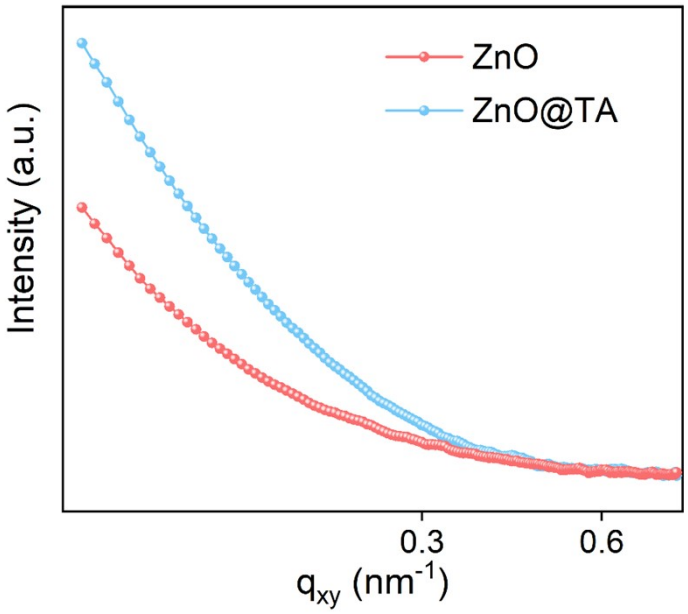

Figure S2. 1D line cuts of the 2D-GISXAS data for the ZnO films before and after tannic acid modification.

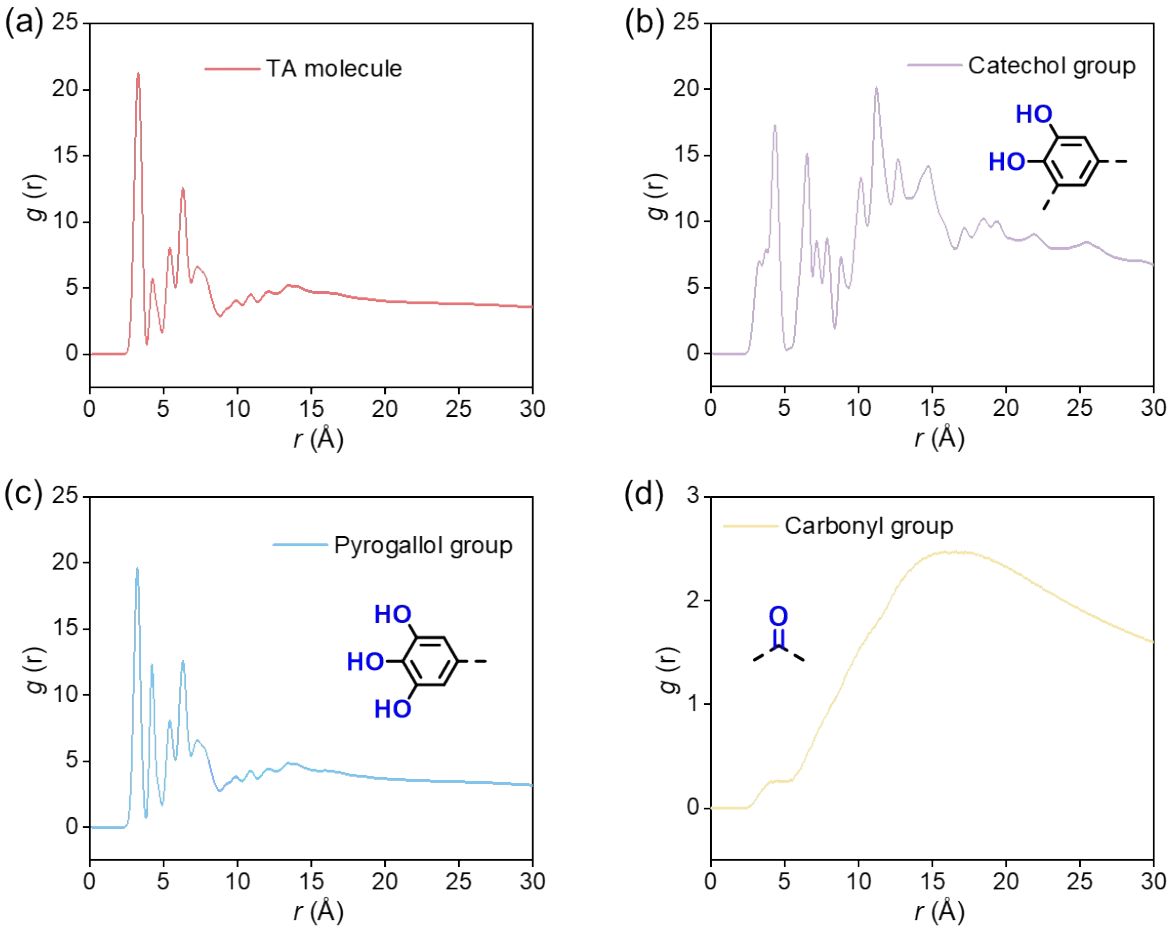

Figure S3. The radial distribution function (RDF) result of (a) tannic acid molecules and (b-d) their functional groups.

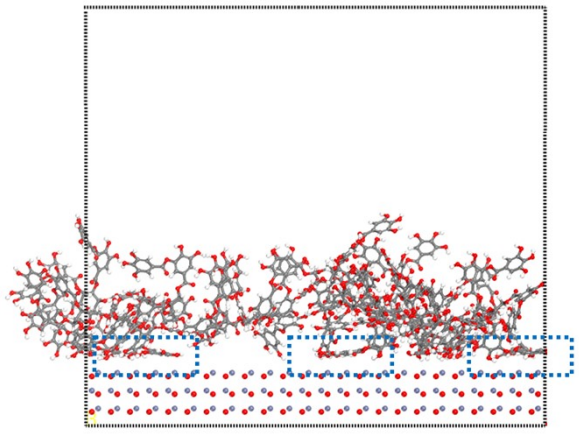

Figure S4. The adsorption configuration of tannic acid molecule.

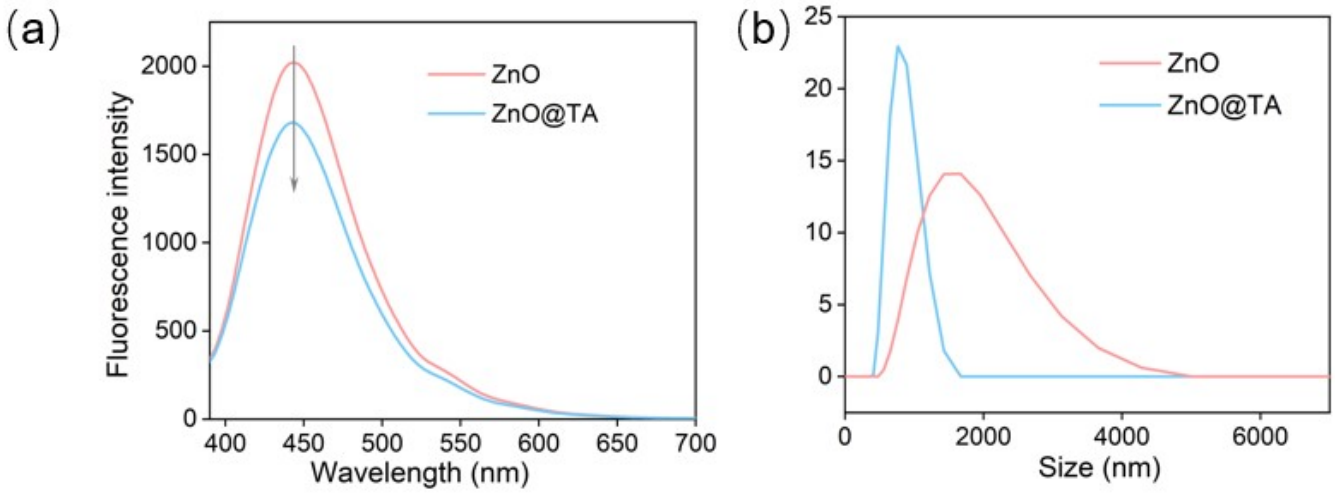

Figure S5. The data of ZnO and ZnO@TA precursor solutions: (a) photoluminescence and (b) dynamic light scattering tests.

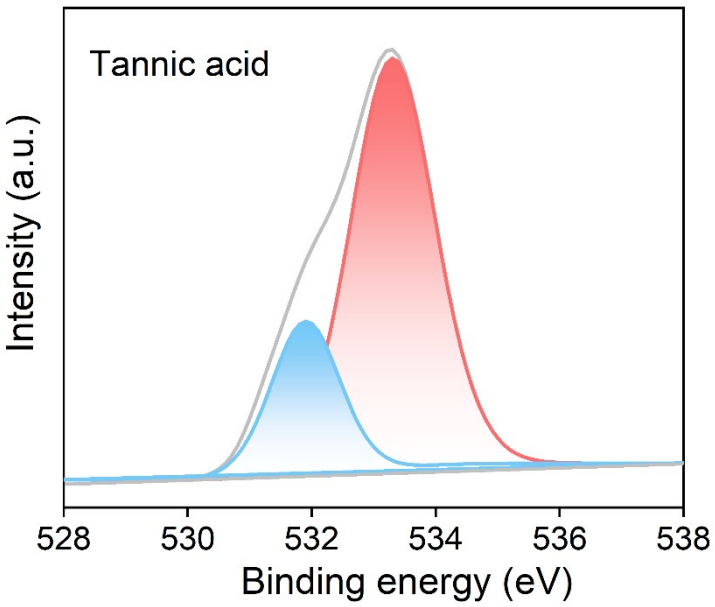

Figure S6. XPS of the TA-only film processed and annealed under 200 °C.

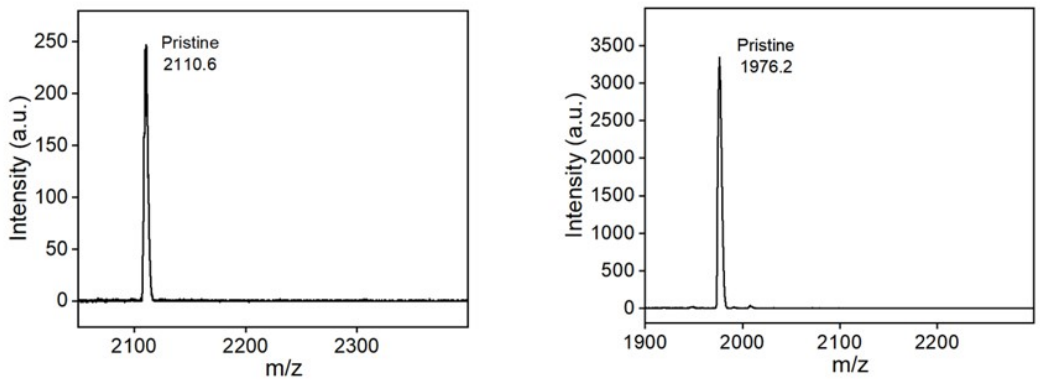

Figure S7. Time of Flight Secondary Ion Mass Spectrometry of Oligomer ADA and DAD.

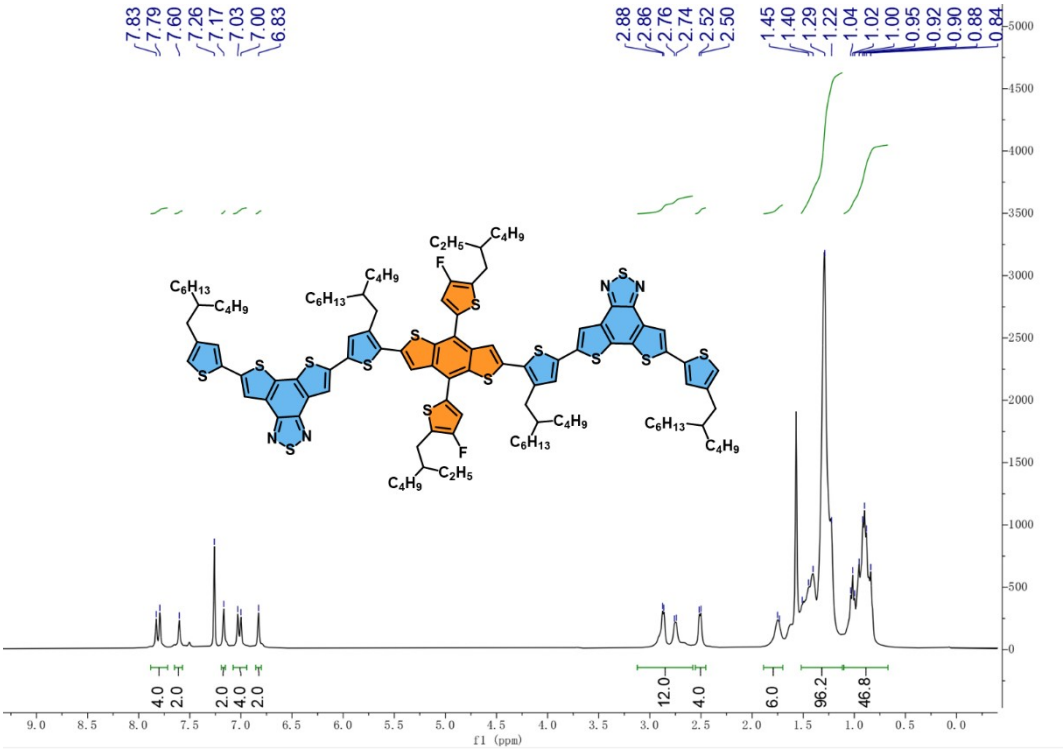

Figure S8. Nuclear magnetic resonance spectra of the ADA-type oligomer of polymer donor D18.

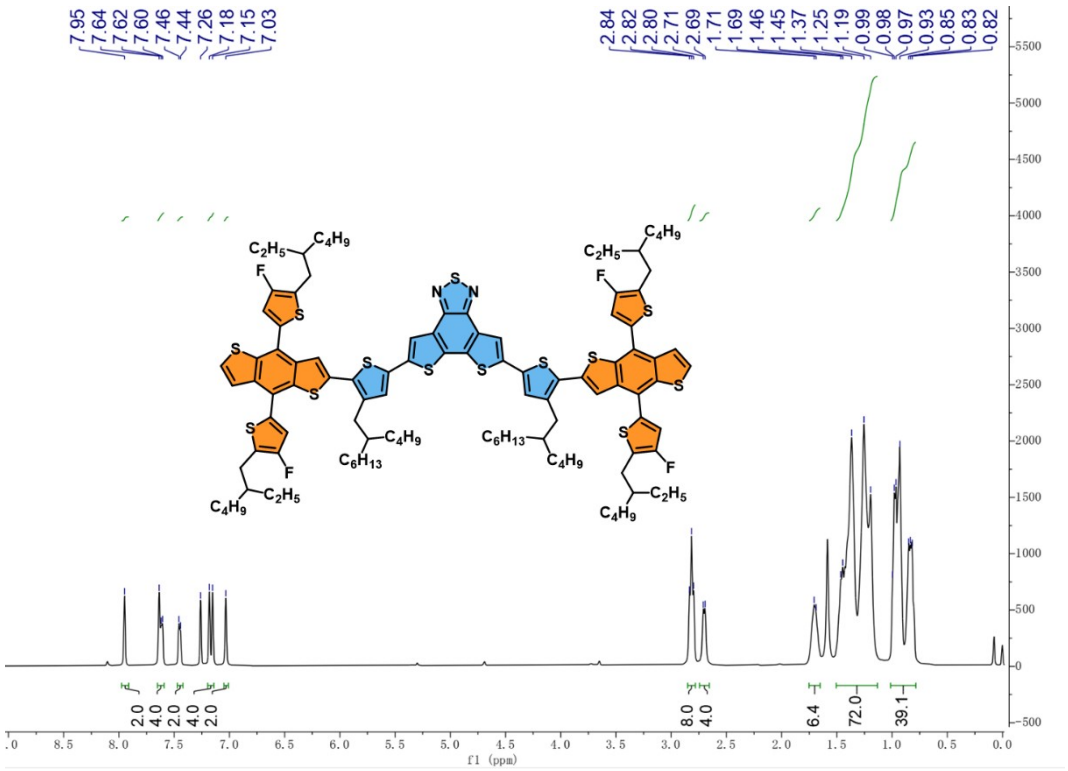

Figure S9. Nuclear magnetic resonance spectra of the DAD-type oligomer of polymer donor D18.

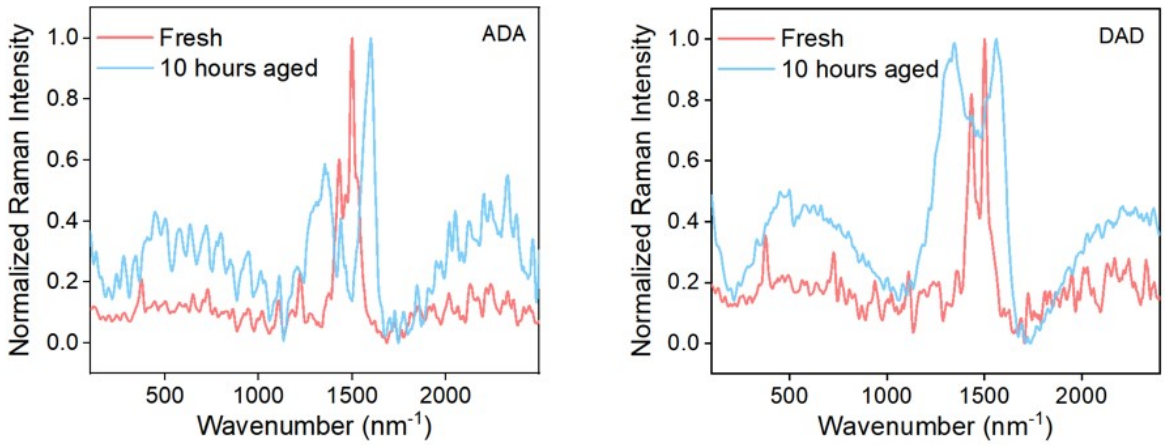

Figure S10. Raman spectra of the oligomer ADA and DAD compounds before and after aging.

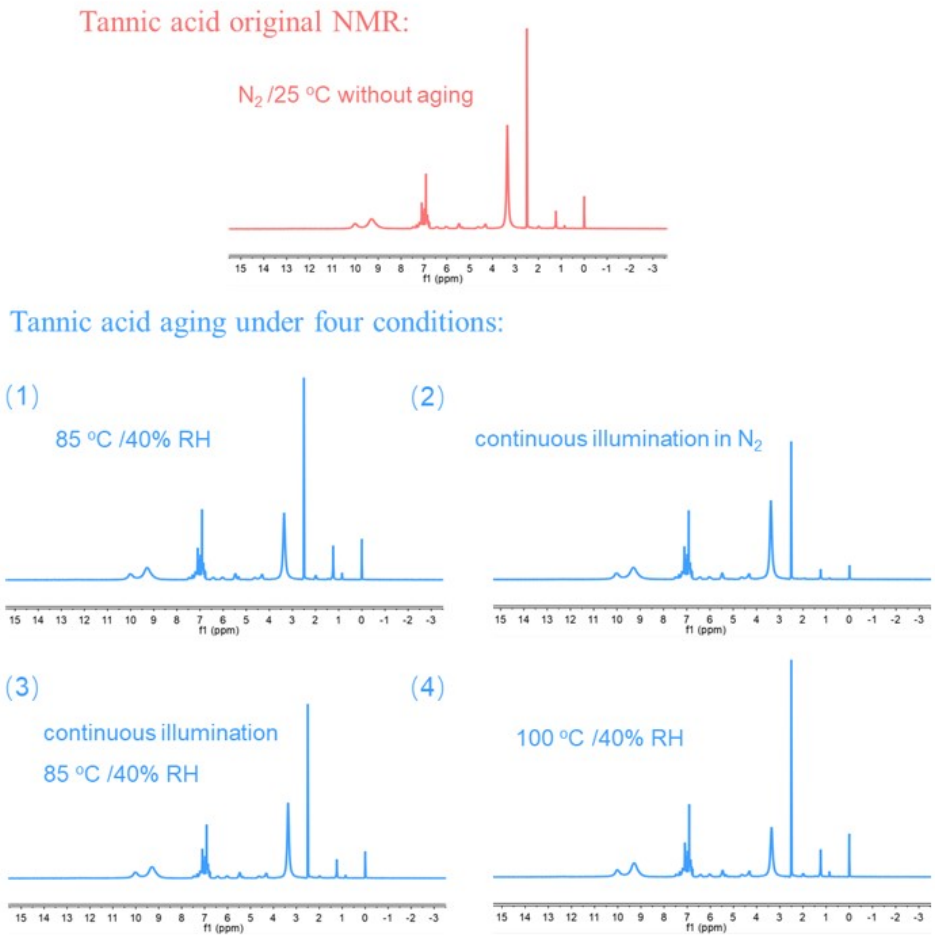

Figure S11. Nuclear magnetic resonance spectra of tannic acid under the pristine state and four different aging conditions (120 hours).

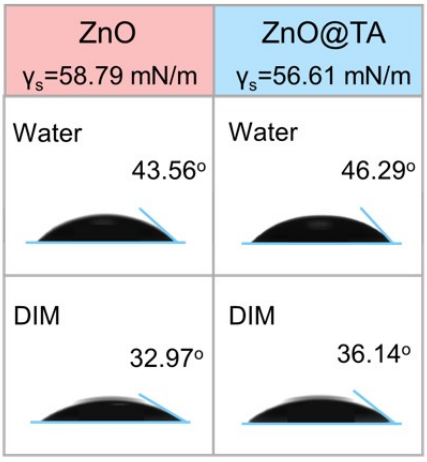

Figure S12. Contact angle of ZnO before and after tannic acid modification.

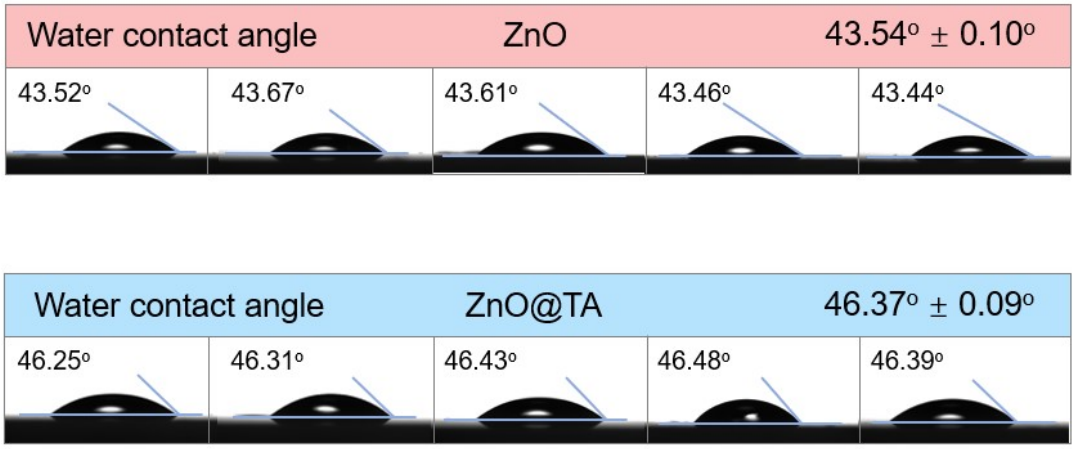

Figure S13. Contact angles of the ZnO thin films and ZnO@TA thin films.

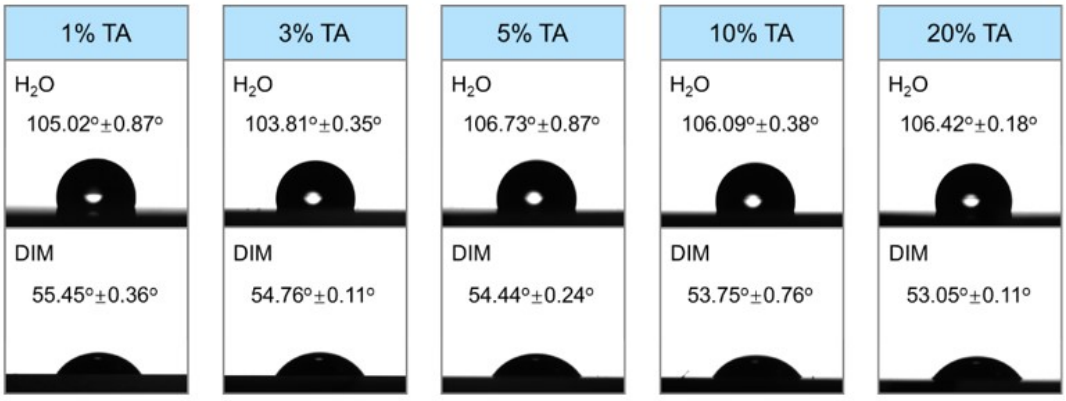

Figure S14. Contact angles of the D18:L8-BO films spin-coated on ZnO films with different TA ratios.

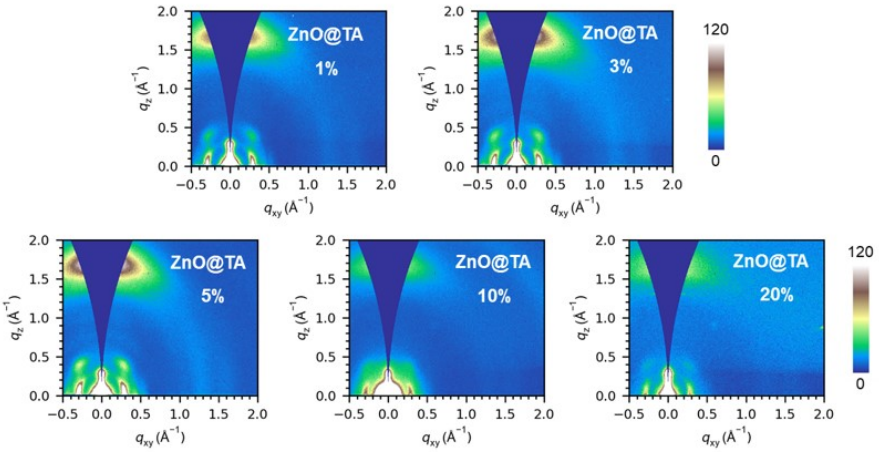

Figure S15. 2D GIWAXS patterns of the D18:L8-BO films spin-coated on ZnO films with different TA ratios.

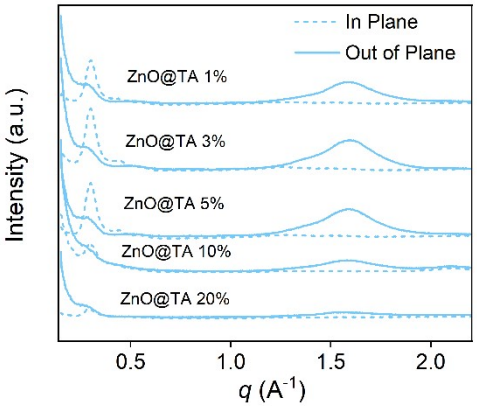

Figure S16. 1D line cuts of photoactive layers of the D18:L8-BO films spin-coated on ZnO films with different TA ratios.

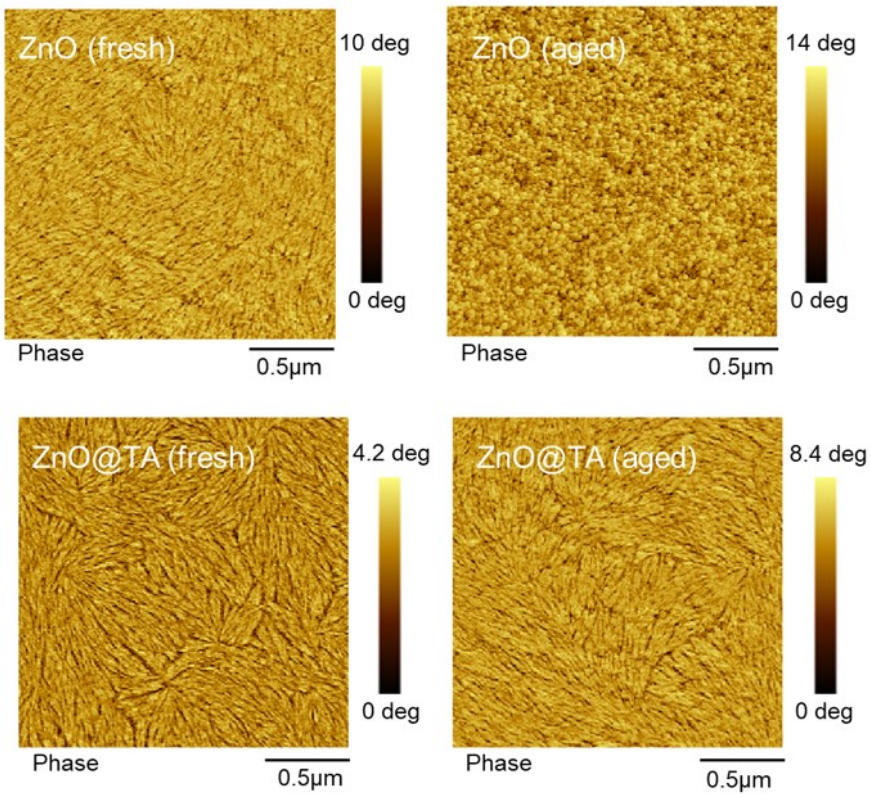

Figure S17. AFM of active layer film based on different ETLs.

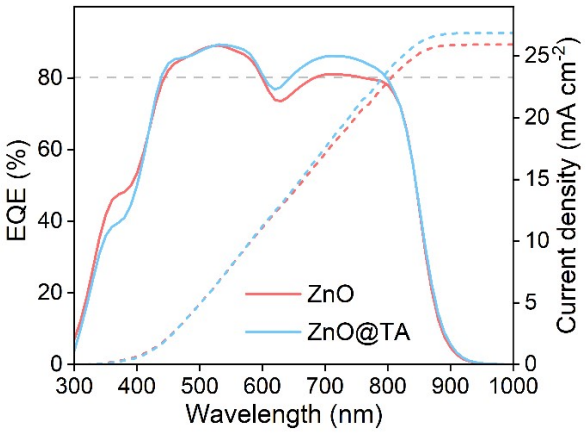

Figure S18. The EQE of the devices of D18:L8-BO before and after TA modification.

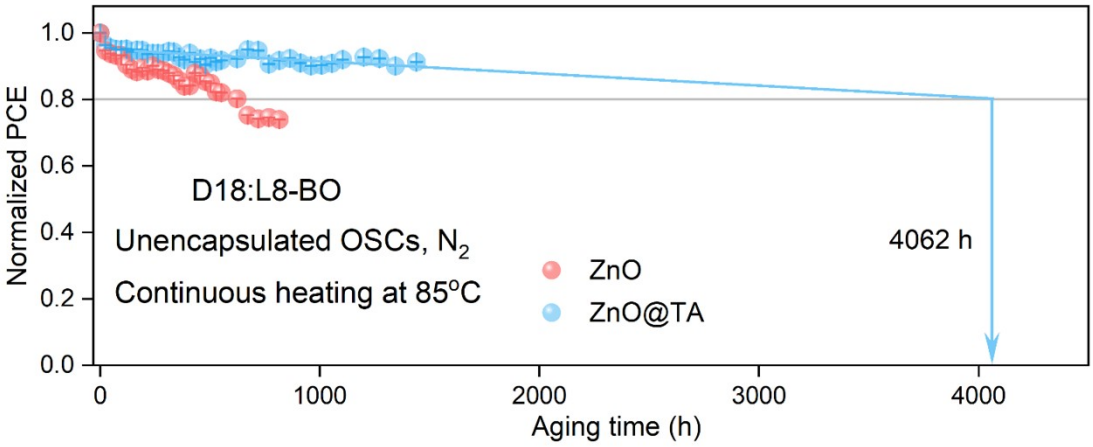

Figure S19. The thermal stability of the devices of D18:L8-BO before and after TA modification. The statistical results, including standard deviation and error bars, are based on five devices.

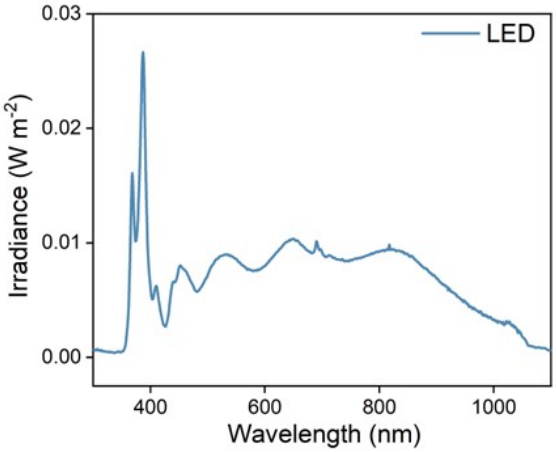

Figure S20. Light spectrum of the LED illumination employed for the operational stability measurements in this study.

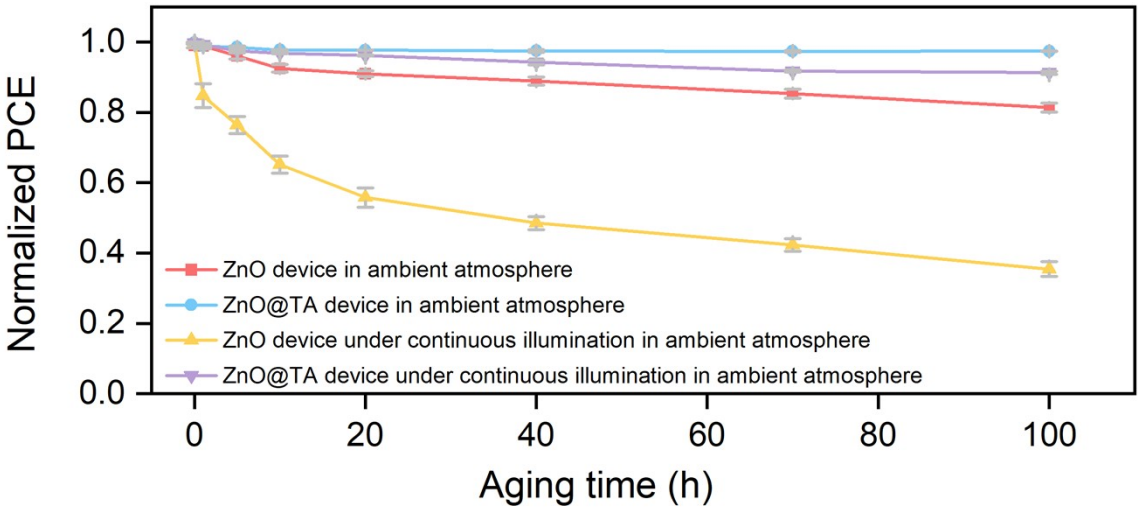

Figure S21. Stability of ZnO and ZnO@TA devices in different ambient atmospheres.

To distinguish between intrinsic/interfacial degradation and oxygen-mediated extrinsic degradation pathways, we supplemented the following experiments. Specifically, we placed ZnO and ZnO@TA devices (five devices per condition) in a humid environment and under continuous illumination in a humid environment, and tested their stability. The experimental results show that the ZnO@TA device placed in a humid environment (without illumination) exhibits the best stability, followed by the ZnO@TA device under continuous illumination in a humid environment, then the ZnO device in a humid environment (without illumination). Finally, the ZnO device under continuous illumination in a humid environment shows the poorest stability (Figure S21). This stability trend indicates the existence of an oxygen-mediated photocatalytic degradation pathway.

Under light conditions and in the ambient atmosphere, ZnO itself is excited to generate electron-hole pairs, and the adsorbed O_2 and H_2O molecules will capture electrons, generating superoxide radicals ($\cdot O_2^-$) or hydroxyl radicals ($\cdot$OH). These highly reactive species will attack the ZnO lattice, accelerating the formation of oxygen vacancies, surface corrosion, and the increase of non-radiative recombination centers. This oxygen-mediated external degradation pathway is the main degradation source. However, TA as a natural polyphenolic compound, has free radical scavenging ability. Therefore, when exposed to light in a humid environment, TA can quench the photogenerated $\cdot O^{2-}$ or $\cdot$OH, thereby inhibiting the photocatalytic corrosion

of ZnO. Thus, the ZnO@TA device shows enhanced stability when exposed to light in a humid environment. By comparing the storage stability of ZnO and ZnO@TA, it was found that the introduction of TA enhanced the storage stability of ZnO in a humid environment. This enhancement is attributed to the interface stabilization effect of TA without illumination.

Overall, the above results demonstrate that the introduction of TA not only enhances the intrinsic stability of ZnO through coordination passivation, but also inhibits the external photodegradation by its free radical scavenging ability.

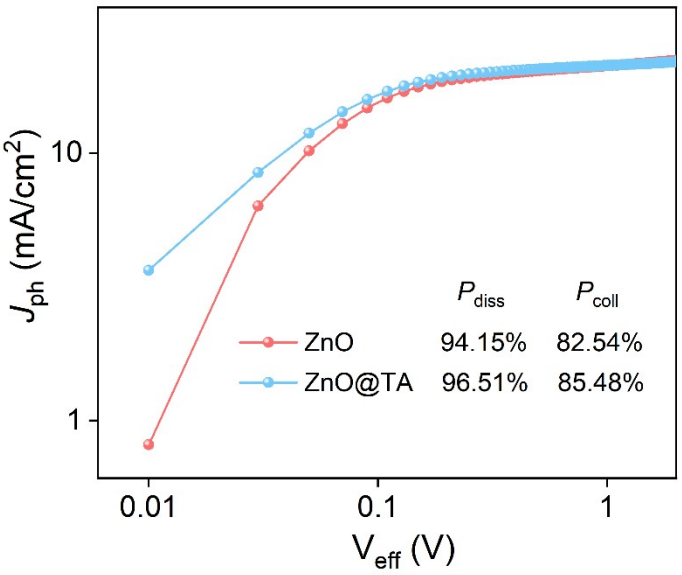

Figure S22. The photocurrent density (J_{ph}) versus effective voltage (V_{eff}) curves of the devices based on different ETL.

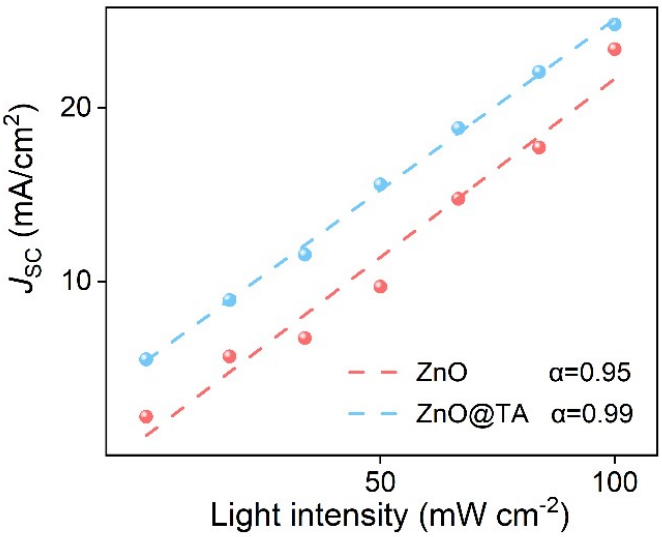

Figure S23. The dependence of J_{SC} on light intensity of the devices based on different ETL**.**

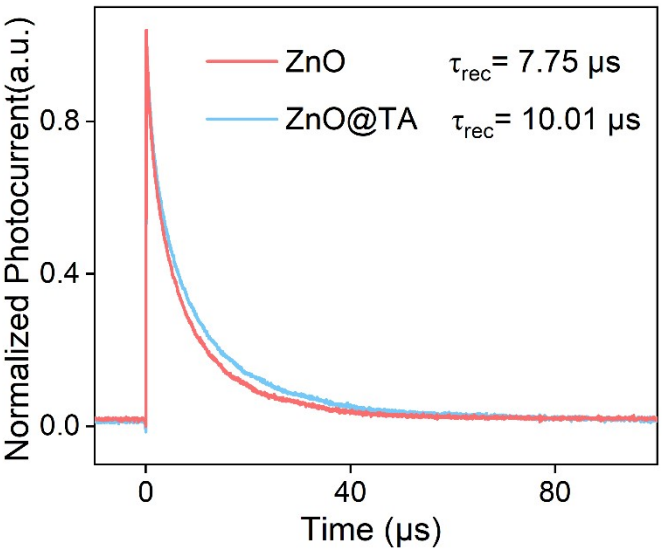

Figure S24. Transient Photovoltage of the devices based on different ETLs.

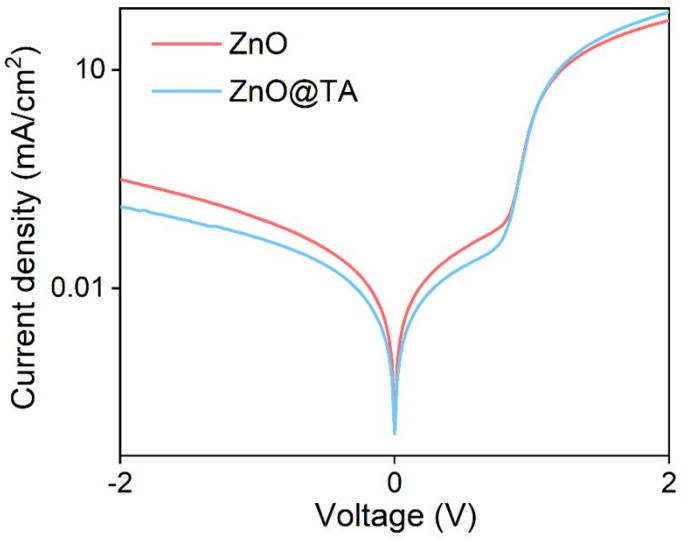

Figure S25. Dark current density of the devices based on different ETLs.

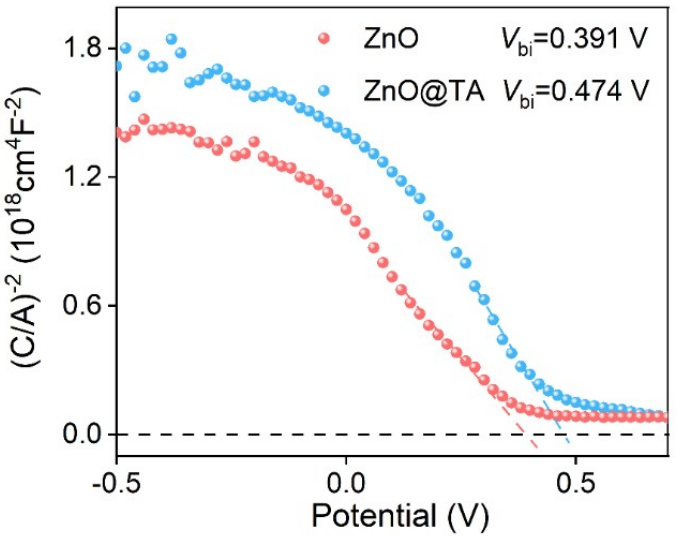

Figure S26. Mott-Schottky analysis of the capacitance-voltage (*C-V*) characteristics in devices based on different ETLs.

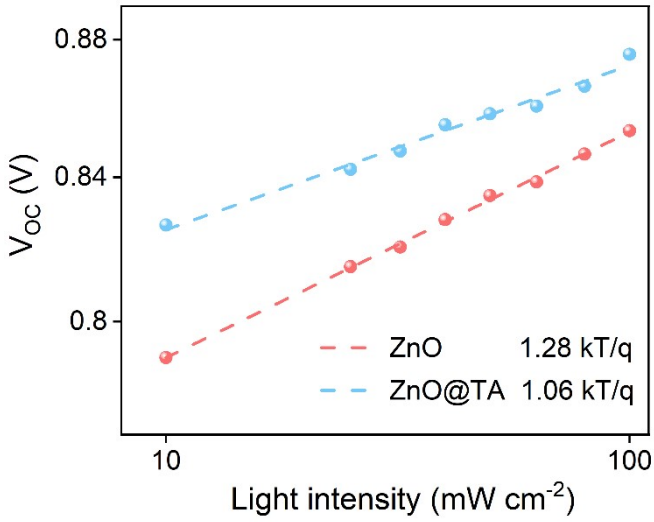

Figure S27. The dependence of V_{OC} on light intensity of the devices based on different ETLs**.**

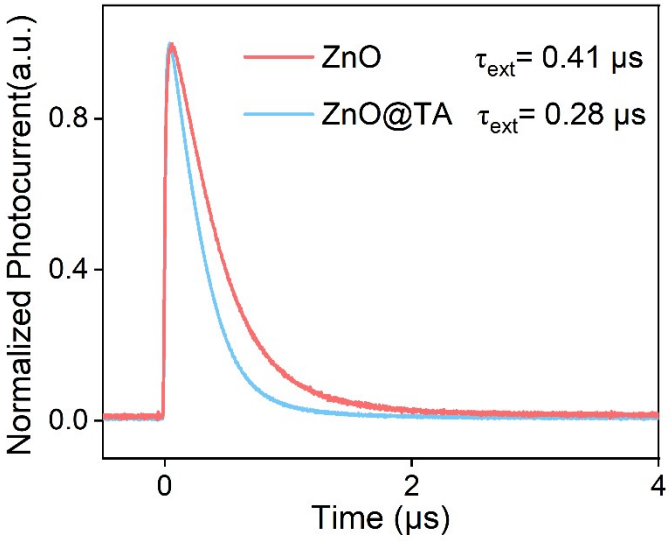

Figure S28. Transient photocurrent of the devices based on different ETLs.

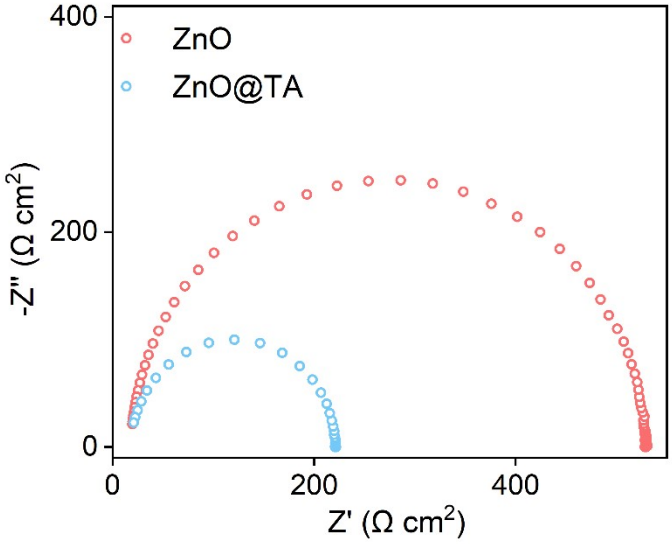

Figure S29. Electrochemical impedance spectroscopy (EIS) analysis of the devices based on different ETLs.

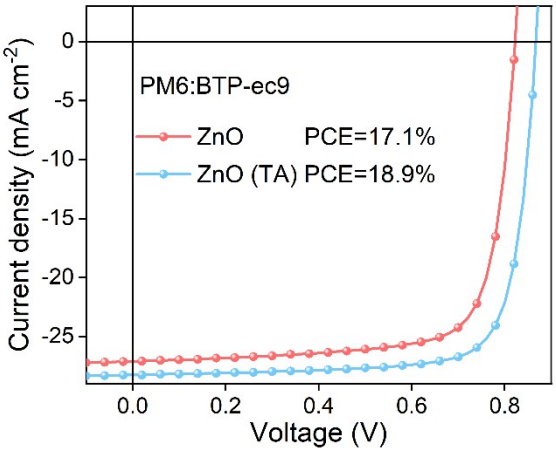

Figure S30. The *J-V* of the devices of PM6:BTP-eC9 before and after TA modification.

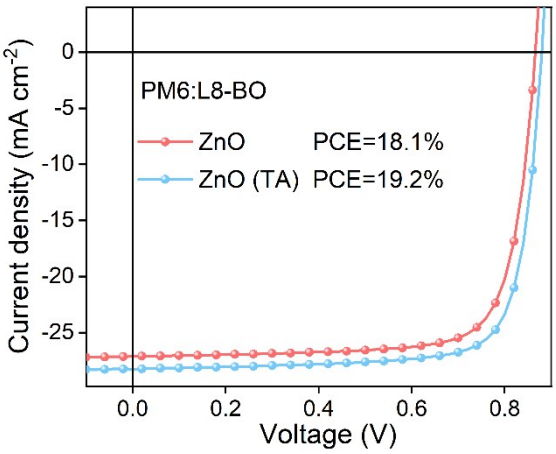

Figure S31. The *J-V* of the devices of PM6:L8-BO before and after TA modification.

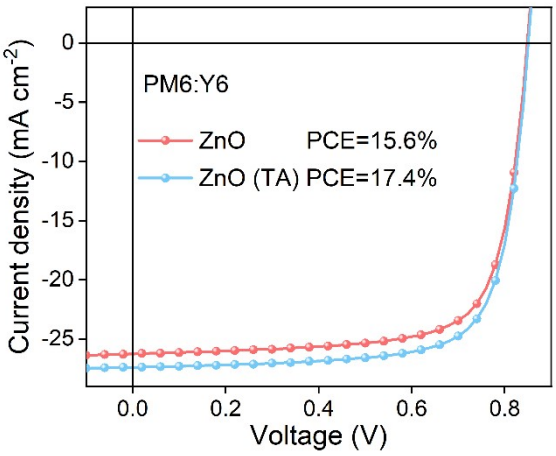

Figure S32. The *J-V* of the devices of PM6:Y6 before and after TA modification.

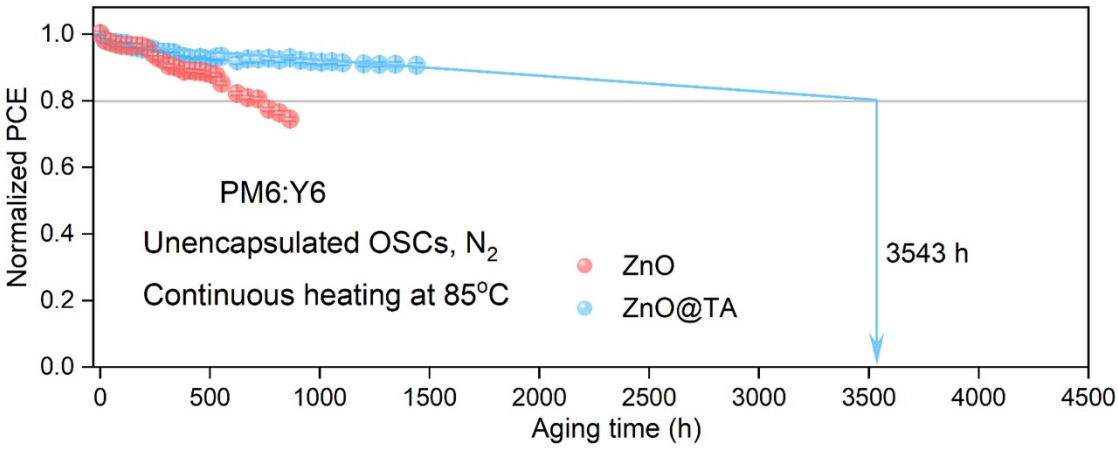

Figure S33. The thermal stability of the devices of PM6:Y6 before and after TA modification. The statistical results, including standard deviation and error bars, are based on five devices.

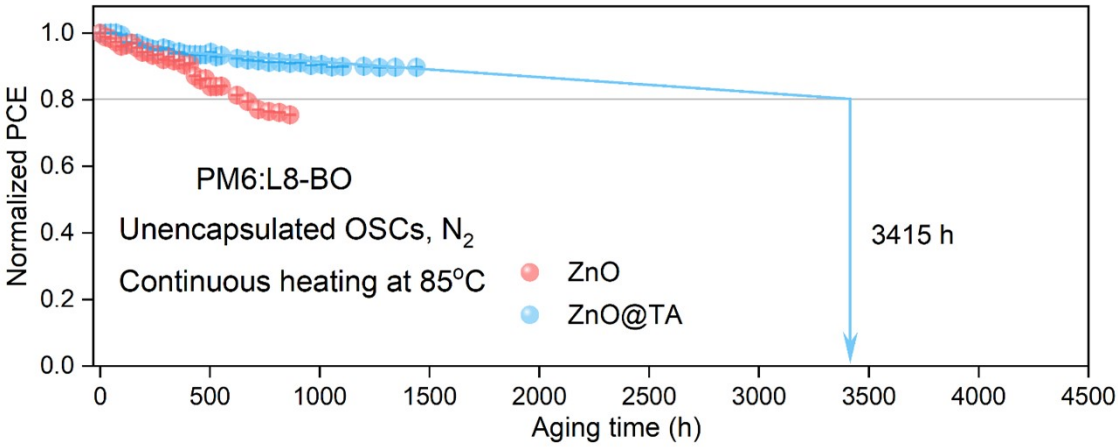

Figure S34. The thermal stability of the devices of PM6:L8-BO before and after TA modification. The statistical results, including standard deviation and error bars, are based on five devices.

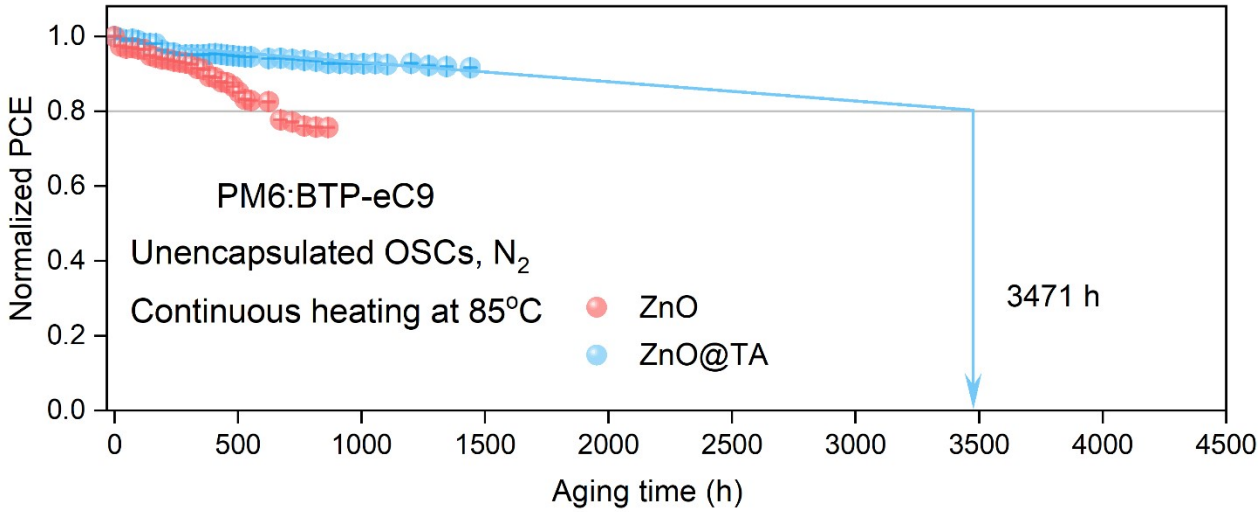

Figure S35. The thermal stability of the devices of PM6:BTP-eC9 before and after TA modification. The statistical results, including standard deviation and error bars, are based on five devices.

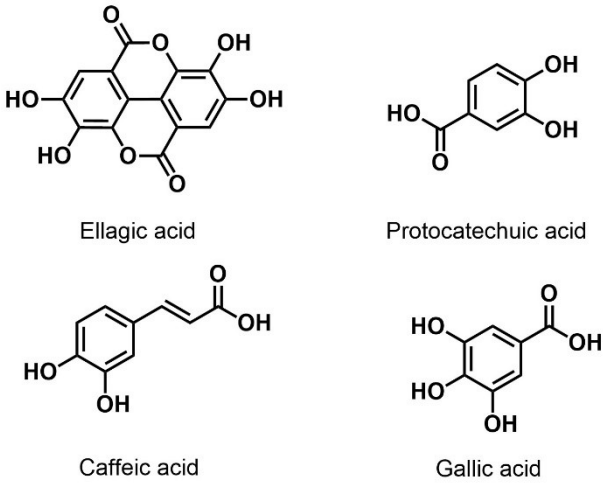

Figure S36. Molecular structures of four small natural molecule compounds.

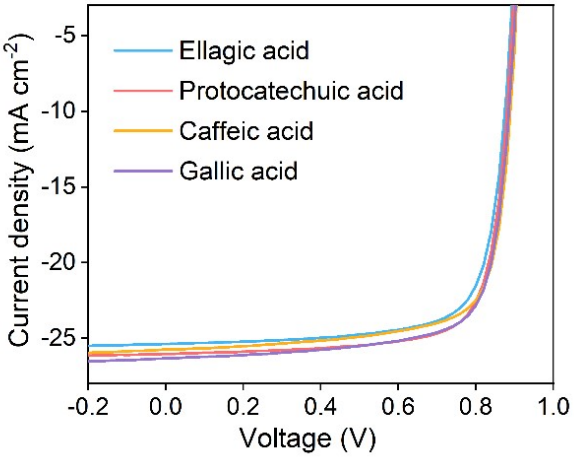

Figure S37. Performance of the devices processed with different natural molecules in D18:L8-BO systems.

Table S1. Calculated interaction energies of the MD simulation.

Energies	TA molecule	Carbonyl group	Pyrogallol group	Catechol group
E_{total} (kcal/mol)		123723.3		
E_{TA}/E_{Group} (kcal/mol)	4125.8	2901.9	3821.1	3190.8
$E_{sub+sol}$ (kcal/mol)		12029.3		
E_{inter} (kcal/mol)	-1231.8	-7.86	-927.1	-296.8

[a]E_{total}, E_{TA} (or E_{Group}), and $E_{sub+sol}$ represent the total energies of the whole system, the TA molecule (or the corresponding functional group), and the ZnO layer (including the substrate and solvent), respectively. E_{inter} denotes the interaction energy between the TA molecule (or different functional groups) and the ZnO layer. Specifically, $E_{inter\text{-}TA} = E_{total} - (E_{sub+sol} + E_{TA})$ and $E_{inter\text{-}G} = E_{total} - (E_{sub+sol} + E_{Group})$.

Table S2. Contact angles and surface tensions of ZnO with and without TA.

Film	θ_{water} (°)	θ_{oil} (°)	γ^d (mJ m^{-2})	γ^p (mJ m^{-2})	γ (mJ m^{-2})
Without	43.56	32.97	77.69	0.62	78.31
With	46.29	36.14	73.97	0.60	74.58

Table S3. Surface tensions of the D18:L8-BO films spin-coated on ZnO films with different TA ratios

Film	θ_{water} (°)	θ_{oil} (°)	γ^d (mJ m^{-2})	γ^p (mJ m^{-2})	γ (mJ m^{-2})
1%	105.1	55.5	17.4	0.5	17.9
3%	103.8	54.8	18.1	0.5	18.6
5%	106.7	54.4	16.5	0.5	16.9
10%	106.1	53.8	16.8	0.5	17.3
20%	106.4	53.1	16.6	0.5	17.2

Table S4. Morphology data of photoactive layers of the D18:L8-BO films spin-coated on ZnO films with different TA ratios

TA ratio	Out-of plane			In-plane		
	q (Å^{-1})	d-spacing (Å)	CCL (Å)	q (Å^{-1})	d-spacing (Å)	CCL (Å)
1%	1.59	3.95	25.4	0.31	20.3	116.2
3%	1.60	3.93	22.4	0.30	20.9	110.4
5%	1.60	3.93	23.1	0.30	20.9	109.9
10%	1.59	3.95	25.1	0.29	21.6	107.3
20%	1.59	3.95	21.9	0.29	21.6	106.7

Sample	Out-of plane			In-plane		
	q (Å^{-1})	d-spacing (Å)	CCL (Å)	q (Å^{-1})	d-spacing (Å)	CCL (Å)
ZnO	1.64	3.83	19.11	0.31	20.26	74.79
ZnO@TA	1.62	3.87	20.67	0.31	20.26	79.24
ZnO(aged)	1.64	3.83	18.92	0.31	20.26	66.31
ZnO@TA (aged)	1.63	3.85	20.19	0.31	20.26	78.21

Table S5. Morphology data based ZnO and ZnO@TA in the blend films.

Table S6. Photovoltaic parameters of the device processed with different preparation method under the illumination of AM 1.5G (100 mW/cm^2).

Preparation method of ETLs	V_{OC} [V]	FF [%]	J_{SC} [mA/cm^2]	PCE [%] [a)]
Spin-coating TA on the ZnO layer	0.521	20.2	14.7	1.5 (1.3± 0.2)
Introducing TA in the ZnO solution	0.903	81.7	27.2	20.1

				(20.0±0.1)

[a)] The average values and standard deviations of five devices are shown in parentheses.

Table S7. Photovoltaic parameters of the devices processed with different TA ratio in PM6:L8-BO system under the illumination of AM 1.5G (100 mW/cm^2).

TA ratio	V_{OC} [V]	FF [%]	J_{SC} [mA/cm^2]	PCE [%] [a)]
0	0.877	78.1	27.2	18.6 (18.2 ± 0.4)
1%	0.879	78.1	27.3	18.7 (18.2 ± 0.5)
3%	0.882	78.2	27.4	18.9 (18.6 ± 0.3)
5%	0.875	76.9	27.2	18.3 (17.8 ± 0.5)
10%	0.874	75.1	27.1	17.7 (17.1 ± 0.6)

[a)] The average values and standard deviations of five devices are shown in parentheses.

Table S8. Photovoltaic parameters of the devices processed with different TA ratios in D18:L8-BO system under the illumination of AM 1.5G (100 mW/cm^2).

TA ratio	V_{OC} [V]	FF [%]	J_{SC} [mA/cm^2]	PCE [%] [a)]
0	0.906	77.8	26.9	18.9 (18.2 ± 0.7)
1%	0.908	77.8	27.0	19.1 (18.7 ± 0.4)
3%	0.903	81.7	27.2	20.1 (20.0 ± 0.1)
5%	0.902	78.4	26.8	18.9 (18.3 ± 0.6)
10%	0.898	77.7	26.7	18.6 (18.1 ± 0.5)

[a)] The average values and standard deviations of five devices are shown in parentheses.

Table S9. The changes in photovoltaic parameters during the aging process.

Devices	V_{OC} [V]	FF [%]	J_{SC} [mA/cm^2]	PCE [%] [a)]
ZnO (before)	0.897	78.7	26.5	18.7 (18.3 ± 0.4)
ZnO (after)	0.854	73.2	22.3	13.9 (13.3 ± 0.6)
ZnO@TA (before)	0.906	81.1	27.2	19.9 (19.7 ± 0.2)

ZnO@TA (after)	0.882	78.3	25.4	17.5 (17.2 ± 0.3)

[a)] The average values and standard deviations of five devices are shown in parentheses.

Table S10. Summary of photovoltaic performance of the binary inverted OSCs based on ZnO as ETL.

	ETL	Active layer	V_{OC} [V]	FF [%]	J_{SC} [mA/cm^2]	PCE [%]	Ref.
1	ZnO/FNEZnP-OE	PTB7-Th:$PC_{71}BM$	0.75	72.13	17.09	9.24	3
2	ZnO/2-naphthol	PTB7:$PC_{71}BM$	0.76	71.00	18.01	9.72	4
3	ZnO/C_{60}-SAM	PTB7-Th:IEICO-4F	0.71	61.18	22.9	10.00	5
4	ZnO/$Zn(OAc)_2$	PM7:IT-4F	0.86	72.00	19.13	11.85	6
5	ZnO/TMAH	PM7:IT-4F	0.85	68.00	18.80	10.87	6
6	ZnO/DMCA	PM6:Y6	0.82	72.00	26.39	15.58	7
7	ZnO/FA	PM6:Y6	0.82	72.40	26.87	15.95	7
8	ZnO/CA	PM6:Y6	0.83	73.80	27.05	16.56	7
9	ZnO/GHK-Cu	PM6:Y6	0.83	74.50	26.63	16.46	8
10	ZnO/ANF	PM6: BTP-eC9	0.84	75.90	26.4	16.90	9
11	ZnO/NMA	D18:N3	0.86	77.30	27.23	18.20	10
12	ZnO/NADH	PM6:L8-BO	0.88	77.99	26.53	18.21	11
13	ZnO/ZrSe2	PM6:L8-BO	0.89	77.34	26.50	18.24	12
14	ZnO/Dex	D18:Y6	0.85	77.52	27.68	18.32	13
15	ZnO/BHT	PM6:L8-BO	0.87	80.72	27.96	18.45	14

Table S11. *J-V* of the different photovoltaic systems processed with and without TA.

Active layer	Fabricating Condition	V_{OC} [V]	FF [%]	J_{SC} [mA/cm^2]	PCE [%]
PM6:Y6	Without	0.839	73.9	25.1	15.6
	With	0.847	74.7	27.6	17.4
PM6: BTP-eC9	Without	0.821	75.9	27.4	17.1
	With	0.859	78.1	28.2	18.9
PM6:L8-BO	Without	0.865	77.3	27.1	18.1
	With	0.881	78.6	27.6	19.2

Table S12. Photovoltaic parameters of the devices processed with different natural molecules in D18 L8-BO systems under the illumination of AM 1.5G (100 mW/cm^2).

Compound	V_{OC} [V]	FF [%]	J_{SC} [mA/cm^2]	PCE [%] [a)]
Ellagic acid	0.900	76.57	25.46	17.5 (17.2 ± 0.3)
Protocatechuic acid	0.902	77.71	26.06	18.3 (18.1 ± 0.2)
Caffeic acid	0.910	76.85	25.79	18.1 (17.6 ± 0.5)
Gallic acid	0.908	76.86	26.34	18.4 (18.3 ± 0.1)

[a)] The average values and standard deviations of five devices are shown in parentheses.

References

[1] P. Hohenberg, W. Kohn, *Phys. Rev.*, 1964, **136**, B864-B871.

[2] W. Kohn, L. J. Sham, *Phys. Rev.*, 1965, **140**, A1133-A1138.

[3] C. Liu, L. Zhang, L. Xiao, X. Peng, Y. Cao, *ACS Appl. Mater. Interfaces*, 2016, **8**, 28225-28230.

[4] P. Fu, X. Guo, B. Zhang, T. Chen, W. Qin, Y. Ye, J. Hou, J. Zhang, C. Li, *J. Mater. Chem. A*, 2016, **4**, 16824-16829.

[5] X. Xu, J. Xiao, G. Zhang, L. Wei, X. Jiao, H.-L. Yip, Y. Cao, *Sci. Bull.*, 2020, **65**, 208-216.

[6] Y. Han, H. Dong, W. Pan, B. Liu, X. Chen, R. Huang, Z. Li, F. Li, Q. Luo, J. Zhang, Z. Wei, C.-Q. Ma, *ACS Appl. Mater. Interfaces*, 2021, **13**, 17869-17881.

[7] S. Yang, H. Yu, *Chem. Eng. J.*, 2023, **452**, 139658.

[8] J. Huang, H. Yu, X. Zhou, *Chem. Eng. J.*, 2022, **428**, 131366.

[9] Q. Zhou, C. Yan, H. Li, Z. Zhu, Y. Gao, J. Xiong, H. Tang, C. Zhu, H. Yu, S. P. G. Lopez, J. Wang, M. Qin, J. Li, L. Luo, X. Liu, J. Qin, S. Lu, L. Meng, F. Laquai, Y. Li, P. Cheng, *Nano-Micro Lett.*, 2024, **16**, 224.

[10] S. Li, Q. Fu, L. Meng, X. Wan, L. Ding, G. Lu, G. Lu, Z. Yao, C. Li, Y. Chen, *Angew. Chem. Int. Ed.*, 2022, **61**, e202207397.

[11] H. Li, S. Yang, H. Yu, *J. Mater. Chem. C*, 2024, **12**, 17429-17438.

[12] H. Li, B. Yu, H. Yu, *Adv. Funct. Mater.*, 2024, **34**, 2402128.

[13] B. Zhang, Z. Pan, W. Li, Y. Zhao, X. Qin, A. Li, M. Lv, X. Qin, W. Guo, Z. He, E. Wang, *Adv. Energy Mater.*, 2025, 2404297.

[14] J. Huang, J. Fu, B. Yuan, H. Xia, T. Chen, Y. Lang, H. Liu, Z. Ren, Q. Liang, K. Liu, Z. Guan, G. Zou, H. T. Chandran, T. W. B. Lo, X. Lu, C.-S. Lee, H.-L. Yip, Y.-K. Peng, G. Li, *Nat. Commun.*, 2024, **15**, 10565.